

Spatial resolution of time-reversal arrays in shallow water

Seongil Kim,^{a)} G. F. Edelmann, W. A. Kuperman, W. S. Hodgkiss, and H. C. Song
Marine Physical Laboratory, Scripps Institution of Oceanography, La Jolla, California 92093-0238

T. Akal

SACLANT Undersea Research Centre, 19138 La Spezia, Italy

(Received 25 September 2000; revised 16 April 2001; accepted 27 April 2001)

A series of time-reversal experiments was performed in shallow water including a range-dependent slope environment. Time-reversal arrays implemented with center frequencies of 445 and 3500 Hz achieved sharp focal regions up to ranges of 30 and 13 km, respectively in 110–130-m shallow water. In this paper, resolution expressions are derived using an image method to describe the focal sizes achieved with time-reversal arrays in various ocean environments. Analysis for the measured data indicates that the focal size approaches the diffraction limit of an array for given waveguide conditions, i.e., waveguide geometry and attenuation. The measured focal size has implications for the maximum achievable resolution of linear matched-field processing which is a computational implementation of the time-reversal process. © 2001 Acoustical Society of America.

[DOI: 10.1121/1.1382619]

PACS numbers: 43.30.Vh, 43.30.Pc, 43.60.Gk [DLB]

I. INTRODUCTION

Recently, acoustic time-reversal mirrors (TRMs) have been demonstrated in the laboratory^{1,2} and in the ocean.^{3–5} Time reversal, also referred to as the process of phase conjugation⁶ in the frequency domain, refocuses the incident acoustic field back to the origin of a probe signal regardless of the complexity of the medium. The focusing or the resolution of a TRM can be described by wave diffraction limits; Rayleigh and Fresnel limits for the transverse and the longitudinal resolution.⁷ In free space, the resolution is described with the physical extent of an aperture, but in an ocean waveguide, the spatial complexity of the sound field resulting from multipath propagation increases the resolution over free space. The purpose of this paper is to describe the resolution accomplished with time-reversal arrays in various ocean environments.

The resolution issue for TRMs is the same as the resolution of matched-field processing (MFP).⁸ While a propagation model is used to match the source-generated sound fields in MFP, the time-reversed signal is physically back-propagated to the original source position using a source–receiver array in a TRM. MFP requires *a priori* environmental information along the propagation path for accurate simulation of wave fields, but such measurements often are not practical. On the other hand, time reversal is an environmental self-adaptive process. Hence, the focal size realized with a TRM can be considered as the maximum achievable resolution of MFP for given waveguide conditions.

Greater performance of an array in a waveguide over the free-space diffraction limit already has been mentioned in the context of MFP using Cramer–Rao bounds,⁸ in ultrasonic experiments,⁹ and in ocean experiments.³ A simple way to look at resolution is to recognize that a water-column-spanning array can produce a focal spot with vertical extent

of approximately the waveguide depth divided by the number of modes, i.e., the shortest vertical wavelength which results from the highest order effective mode. In this paper we present foci achieved with low- (445 Hz) and high-frequency (3500 Hz) TRMs in various ocean environments. Resolution expressions using an image method are derived for a Pekeris waveguide and a wedge ocean to describe the measured focal sizes. This description provides physical and quantitative insight into how waveguide parameters such as geometry and attenuation affect resolution in MFP as well as in the time-reversal process.

In this study, we do not consider dynamic ocean effects^{10,11} under the assumption that the ocean is static during the time between the forward propagation and the time-reversal backpropagation. The measured data presented here were selected from the signals which were backpropagated within 2 min of reception. The possible components of time-dependent ocean variations on this time scale are surface and internal waves. Since the observed sound-speed profiles during the experiments were strongly downward refracting and the periods of internal waves are much longer than this time scale, the effect of these dynamic feature is assumed to be negligible.

In the next section, time-reversal experiments are briefly described and the measured foci in various ocean environments are presented. In Sec. III, we formulate the equations describing time-reversal focusing in free space and ocean waveguides. The equation describing the focused acoustic field is interpreted as the near-field beam pattern of an array. In Sec. IV, the transverse (doped) and longitudinal (range) resolution expressions are derived from the beam-pattern equations. The bottom attenuation serves as an aperture shading and reduces the effective aperture of TRM. In Sec. V the measured time-reversal foci are compared with the theory.

^{a)}Electronic mail: seongil@mpl.ucsd.edu

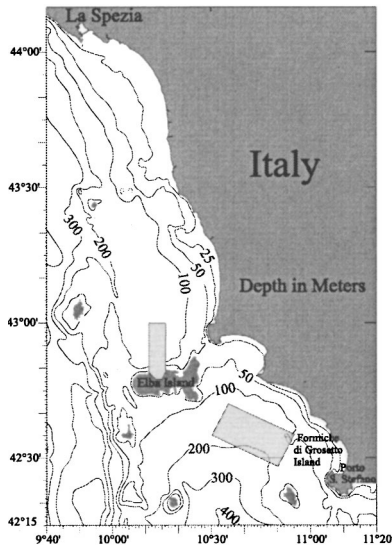


FIG. 1. Locations of the time-reversal experiments. In April 1996 and May 1997, low-frequency (445-Hz) experiments were performed near the Formiche di Grosseto. In July 1999, a high-frequency (3500-Hz) experiment was carried out both north of Elba and in the Formiche area.

II. TIME-REVERSAL EXPERIMENTS

A. Experimental setup

Here, we briefly describe the experimental equipment and the environmental conditions of the sites where the time-reversal experiments were performed.^{3–5} Refer to the cited references for the detailed descriptions of hardware and ocean environments. The important point is the difference in geoacoustic properties between the Formiche and Elba areas, which resulted in different attenuation and focal sizes.

We performed a series of time-reversal experiments in two areas (near Formiche and Elba islands) off the west coast of Italy (see the boxes in Fig. 1). The two experimental sites have very different seabed properties.^{12–15} The area near Formiche is a relatively flat environment with water depth of about 120–130 m. The sediment contains a homogeneous clay layer with thickness varying between 4 to 8 m. Since the sound speed in the sediment layer is less than the water column (slow bottom), most of the acoustic energy penetrates into the sediment layer and interacts with the silt sub-bottom resulting in large attenuation. The area north of Elba has 2- to 3-m-thick sand sediments where sound speed in the sediment is known to be greater than that of the water column (fast bottom). The water depth in the flat Elba area is about 110–120 m. Experiments were performed both in the flat area and the slope environment close to the island. In the slope environment, the water depth decreases from 115 to 0 m in about a 10-km range. The slope is steeper near the island ($\sim 2^\circ$). Figure 2 shows the two-layer geoacoustic models for these areas.^{14,16}

Figure 3 shows the experimental setup for acoustic and oceanographic measurements. A TRM was implemented with a vertical source–receiver array (SRA). The SRA receives an incident signal from a probe source (PS) and retransmits the time-reversed signal to the receiving array which is collocated with the PS. In April 1996 and May 1997, a TRM was deployed near Formiche di Grosseto con-

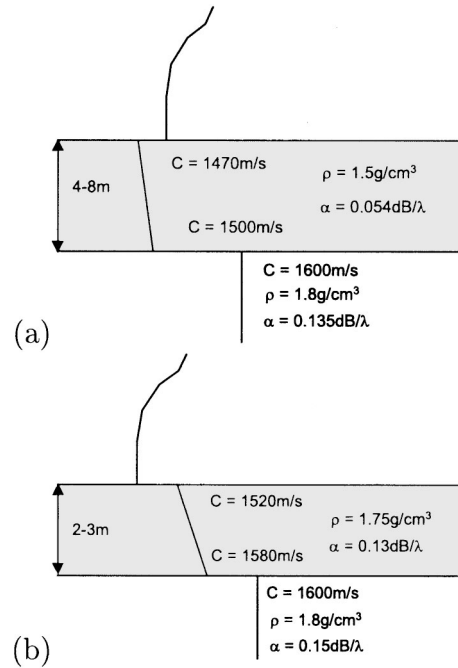


FIG. 2. Two-layer geoacoustic models for the experimental area: (a) Formiche (slow bottom) and (b) North Elba (fast bottom).

sisting of a 77-m SRA with 20 hydrophones and 20 contiguously located slotted cylinder sources with a frequency of 445 Hz. Each element of the SRA was operated at a nominal source level of 160 dB/1 μ Pa with 50-ms pure-tone pulses. The SRA was hardwired to the island for time-reversal processing. A PS was located in the vicinity of a 48-element vertical receive array (VRA) which radio telemetered all data back to the R/V ALLIANCE. The July 1999 experiment was performed with a center frequency of 3500 Hz both north of Elba and in the Formiche area. The experimental setup was similar to the previous ones but the SRA had 29 transducers spanning a 78-m aperture. The source level of the SRA was 178 dB/1 μ Pa and the nominal pulse lengths were 2 and 10 ms at 3500 Hz. The VRA covered 93 m of the water column with 32 hydrophones. This time, both the VRA and SRA were radio linked to the R/V ALLIANCE.

Oceanographic measurements included a wave rider, current meters, and conductivity-temperature chains. Sound-speed profiles (SSP) were measured frequently by conductivity-temperature-depth (CTD) casts. The SSPs collected over the experiment period indicate the variability of the upper water column, especially in the thermocline region (Fig. 4). The downward-refracting sound-speed structure resulted in substantial interaction of the sound field with the ocean bottom.

B. Measured time-reversal foci

In this section, we describe the measured focal structure. Of interest are focal size variations: (1) with frequency; (2) with waveguide conditions; and (3) with range. The results presented in this paper are limited to the vertical focal structure. Although the horizontal focal structure also was investigated in the experiments, we do not include the results in this study since the measured data did not cover the whole

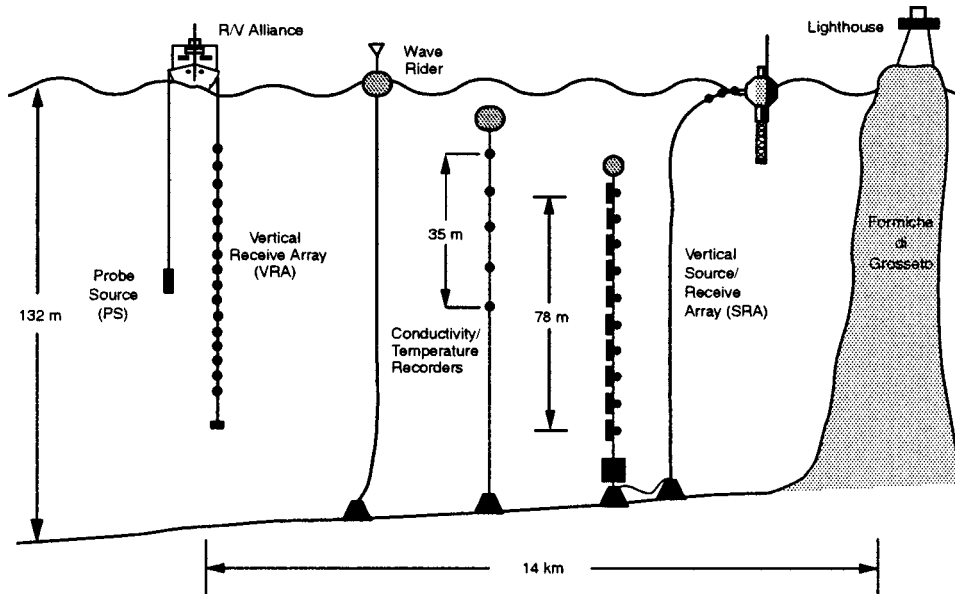


FIG. 3. Experimental setup for the July 1999 high-frequency (3500-Hz) time-reversal experiment near Formiche di Grosseto. The time-reversal array (vertical source–receiver array) consisted of 29 transducers with inter-element spacing 2.786 m spanning 78 m of the water column. Oceanographic measurements included regular CTDs, a wave rider buoy, conductivity-temperature recorders, current meters, etc. The setups were similar for the low-frequency (445-Hz) experiments except that the source–receiver array had 20 elements spanning an aperture of 77 m. The VRA covered 93 m of the water column with 32 hydrophones in the high-frequency experiment and 96-m of one water column with 48 hydrophones in the low-frequency experiments.

scale of the horizontal resolution and the elapsed time over which the measurements were made does not guarantee static ocean conditions.

The focused acoustic fields were measured by the VRA. The received signals were bandpass filtered and envelopes of each signal was extracted using a discrete Hilbert transform.¹⁷ A spline interpolation scheme was applied in depth direction for the intensity data of time vs depth. The depth focal size was defined at the 3-dB down points from

the peak level with integrations for the pulse length.

In free space, the transverse focal sizes are directly proportional to the wavelengths or inversely to the frequencies. In a waveguide, the different loss mechanisms at the boundaries between low- and high-frequency propagation sometimes prevent the focal sizes from being proportional to the wavelengths. Figure 5 shows the results for two different frequencies measured in the Formiche area (130-m water depth). The foci were observed at a range of 15 km with a 50-ms pure-tone pulse with a center frequency of 445 Hz [Fig. 5(a)] and at a range of 12.73 km with a 10-ms pure-tone pulse with a center frequency of 3500 Hz [Fig. 5(b)]. The probe source depths were 80 m for both cases. The vertical focal sizes are 20 and 7.5 m, respectively, with a size ratio of 2.7 between the low-frequency and the high-frequency focus. In this case the ratio of wavelengths is 7.8, which is substantially different from the ratio of focal sizes.

The waveguide attenuation and geometry play important roles for determining the focal size. Figure 6 represents the foci obtained in three different environments: (a) Formiche area (slow bottom); (b) flat Elba area (fast bottom); and (c) sloping Elba area. The water depths were 130 m in the Formiche area and 120 m in the flat Elba area. In the slope experiment, the SRA was located in 120-m-deep water and the probe source in 33-m-deep water. The bathymetry sloped upwards about 1° – 2° from shallow water to the island. The focus was realized with 2-ms rectangular pulses at a center frequency of 3500 Hz. The ranges were 7.9, 7.4, and 9.6 km, and the probe sources were 70, 60, and 22 m deep, respectively. The vertical focal sizes at the 3-dB down points are 6.3, 3.8, and 1.7 m. The main reason for the different focal sizes is the difference in bottom attenuation between the Formiche and Elba areas and additional geometric effects in the sloping environment. The slow bottom in the Formiche area causes greater attenuation than the fast bottom in the Elba area. The geometric effects in the slope environment are discussed in Sec. IV.

The spatial focus broadens with range due to mode stripping.⁴ Figure 7 shows the foci achieved with different

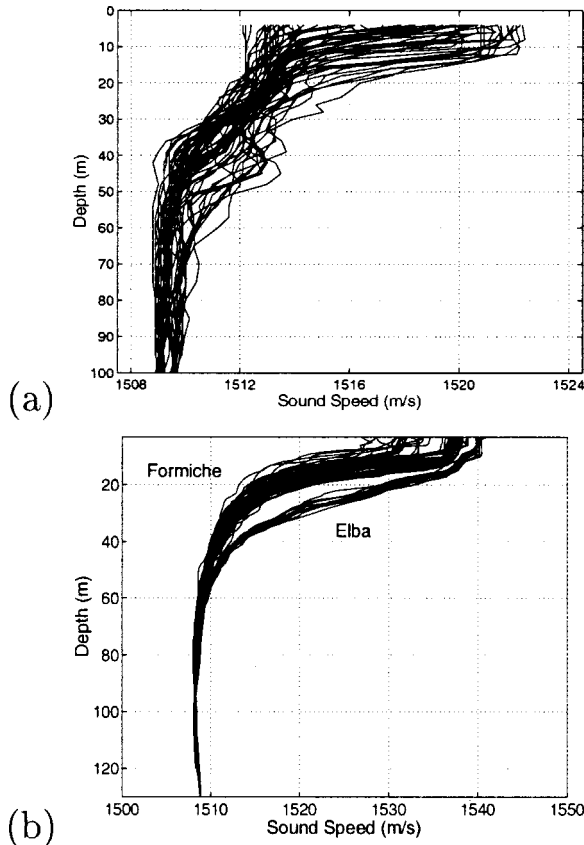


FIG. 4. Sound-speed profiles measured with CTD casts from the R/V ALLIANCE: (a) in the 1997 experiment and (b) in the 1999 experiment.

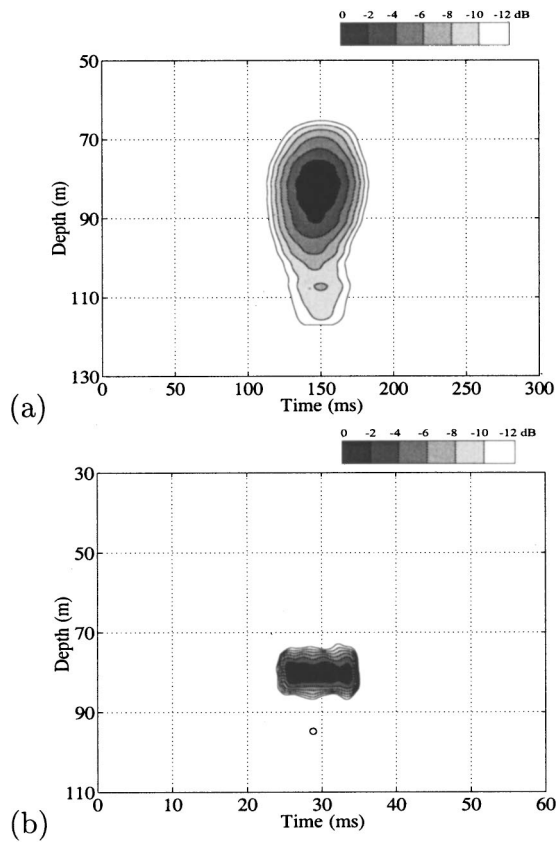


FIG. 5. Measured time reversal foci: (a) for 445 Hz with a 50-ms pulse at 15 km and (b) for 3500 Hz with a 10-ms pulse at 12.73 km. The source depths were both 80 m. The focal size is proportional to the wavelength but the relationship is not linear due to the differential effect of attenuation with frequency in the ocean bottom.

ranges in the Formiche area. The focus was observed out to 30 km at 445 Hz with a 50-ms pulse and 13 km at 3500 Hz with a 2-ms pulse. The focal size changes from 12 m at 4.5 km to 28 m at 30 km for 445 Hz and from 3.8 m at 2.2 km to 7.3 m at 12.8 km for 3500 Hz, which shows that the focal size is somewhat proportional to the square root of range.

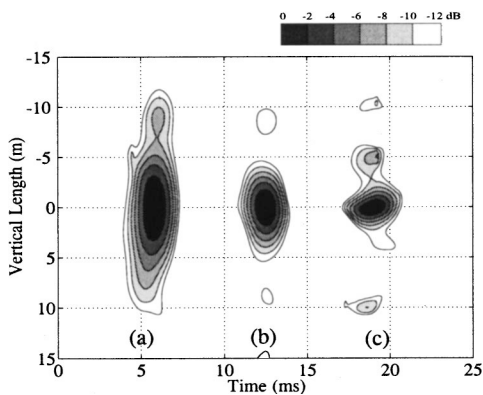


FIG. 6. Measured foci for 3500 Hz with a 2-ms pulse in three different environments: (a) Formiche area at 7.9 km range with PS at 70-m depth; (b) flat Elba area at 7.4 km with PS at 60-m depth; and (c) sloping Elba area at 9.6 km range with PS at 22-m depth in 33-m water depth. The main reasons for the different focal sizes are due to the difference in bottom attenuation between the Formiche and flat Elba areas and additional geometrical effects in a sloping environment.

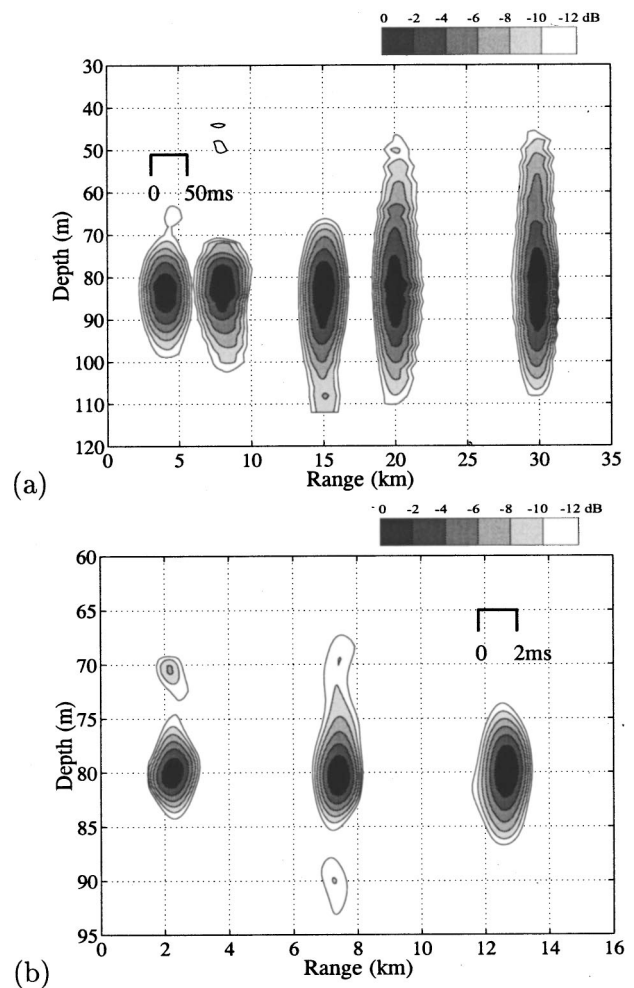


FIG. 7. Measured focal sizes at different ranges from SRA: (a) for 445 Hz and (b) for 3500 Hz. As expected, the spatial focus in depth broadens with range due to mode stripping. Note the different scales in pulse length, range, and depth.

III. TIME-REVERSAL FOCUSING WITH A LINE ARRAY

A. Free space

Here, we briefly review the time-reversal focusing with a line array in free space.¹⁸ Figure 8 shows a line array of an aperture L associated with a spherical coordinate. The pressure field received at a field point (r, φ) from an element dz of the array is

$$dp = \frac{S(z)}{l} \exp(jkl) dz, \quad (1)$$

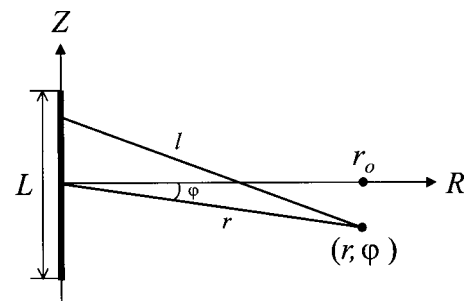


FIG. 8. A line array of aperture L associated with spherical coordinate.

where $S(z)$ is either a source amplitude or an aperture shading along the array, $j = \sqrt{-1}$, k is the wave number, and l is the path length from a source point to a receiver point. Inserting a phase-conjugated probe signal $A \exp(-jkl_0)/l_0$ into $S(z)$, the pressure field observed at a field point (r, φ) from the time-reversal array is

$$p(l) = \int_{-L/2}^{L/2} \frac{A}{l_0} \exp jk(l - l_0) dz, \quad (2)$$

where A is the amplitude of the probe source and l_0 is the distance from a probe source to an element of the array. The path length is given by

$$l^2 = r^2 + z^2 + 2rz \sin \varphi, \quad (3)$$

and using a binomial expansion, l can be represented as

$$l = r + z \sin \varphi + \frac{z^2}{2r} \cos^2 \varphi - \frac{z^3}{2r^2} \sin \varphi \cos^2 \varphi + \dots \quad (4)$$

In the near field ($1.356L < r < kL^2/2$),¹⁹ only the first term of the expansion is necessary for approximating the amplitude term in Eq. (2), but we need to consider to the second-order term for the phase term since a small path-length difference causes a large phase difference. With this Fresnel approximation¹⁹ and the probe source position of $(r_0, 0)$, Eq. (2) becomes

$$p(r, \varphi) = A \frac{\exp jk(r - r_0)}{rr_0} \int_{-L/2}^{L/2} \exp \left[jk \frac{z^2}{2} \left(\frac{\cos^2 \varphi}{r} - \frac{1}{r_0} \right) \right] \times \exp(jkz \sin \varphi) dz. \quad (5)$$

This is a one-dimensional spatial Fourier transform expression which can be interpreted as a near-field directional function (beam pattern) of a line array lying along the z axis. The exponential terms associated with r become unity with $r \rightarrow r_0$ and $\varphi \rightarrow 0$, i.e., to the probe source position, indicating that the time-reversal propagation compensates for the quadratic phase differences caused by the path-length differences. Along the locus of points $r = r_0 \cos^2 \varphi$ the field becomes exactly that of a uniform line array at infinity (Fraunhofer zone), i.e., the far-field beam pattern. Although the focal surface bows slightly with the z direction, it is not enough to be of concern for a small φ . Ignoring the amplitude spreading term A/rr_0 , the far-field beam pattern near the focal region is

$$D(\chi) = \int_{-L/2}^{L/2} \exp(j\chi z) dz, \quad (6)$$

where $\chi = k \sin \varphi$. Notice that the beam pattern along the z direction is determined by the angle φ ; in other words, the relative position difference between the probe source and the observation field point, and by the wave number k .

B. Ocean waveguide

Similarly, we can define a time-reversal focusing in a ocean waveguide using an image method.²⁰ Although the image method is only applicable to the waveguide with a homogeneous water column, the method well describes most shallow-water propagations. The ocean surface is assumed to

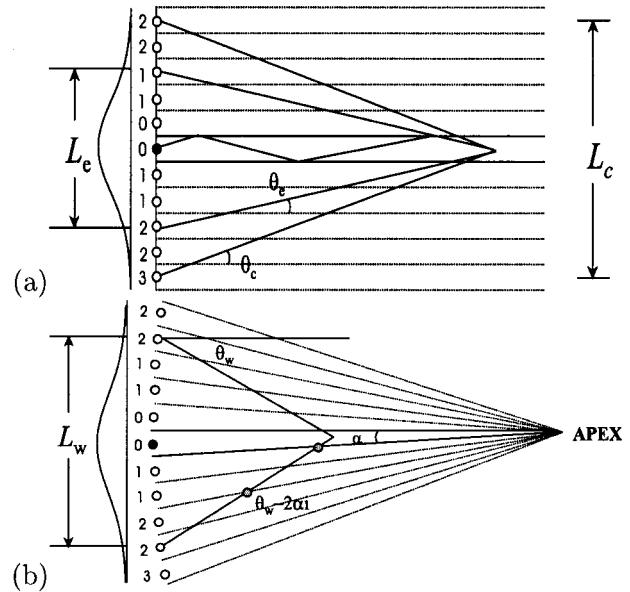


FIG. 9. Schematic of image arrays: (a) for a Pekeris waveguide and (b) for a sloping environment. The image aperture L_c is determined by the critical angle (θ_c) of the bottom. The effective aperture L_e is smaller due to attenuation in the ocean bottom which causes shading of the image sources. In a sloping environment, the grazing angle changes by 2α for each bounce with the bottom which results in a difference in the effective aperture L_w . The labels at the image sources indicate the number of interaction with the bottom.

be a perfect reflector, while the bottom is an interface which reduces the pressure amplitude by a reflection coefficient which can be determined by the geoacoustic properties of the bottom. As a consequence of multiple reflection from the surface and bottom boundaries, the field at the receiver is represented as the summation of contributions from image sources (Fig. 9). Each image source represents the image of a time-reversal array which spans the whole water column of the waveguide. The higher angle image has more interactions with the bottom and contributes less to the total field.

If we label the images with the number of interactions they have with the bottom (Fig. 9), the distance l_i for each set of two images whose contributions make i interactions with bottom can be approximated as

$$l_i \approx r^2 + (2Di)^2 + 2r(2Di) \sin \varphi. \quad (7)$$

This is same as Eq. (3) except z is replaced with $2Di$. Although the exact path length is important to describe one-way acoustic propagations, the exact locations of the array elements are not important for the calculation of the time-reversed field since the time-reversal process compensates for the phase delays caused by the path differences to each image.⁶ The pressure field received by an image source from a point source located in a waveguide is

$$p_i = \frac{S(\theta_i) V(\theta_i)^{i\text{th}}}{l_i} \exp(jkl_i), \quad (8)$$

where $S(\theta_i)$ is the source amplitude, $V(\theta_i)$ is the reflection coefficient of the bottom, θ_i is the grazing angle of the image source which has i interactions with bottom, and k is the wave number. $V(\theta_i)^{i\text{th}}$ is the accumulated attenuation with i -time bottom interactions. The pressure field observed at a

field point after a time-reversal process with a probe signal $AV(\theta_i)^{\text{th}} \exp(jkl_{0i})/l_{0i}$ can be represented as the summation of contributions from each image source as

$$p(l) = A \sum_{i=-\infty}^{\infty} \frac{|V(\theta_i)|^{2|i|}}{l_i l_{0i}} \exp jk(l_i - l_{0i}), \quad (9)$$

where l_i^0 is the distance from a probe source to the i th image source. Negative values in i mean the contribution from the image sources corresponding to negative θ . In the above equation we used $V(\theta_i)V(\theta_{0i})^+ \approx |V(\theta_i)|^2$, where θ_{0i} is the grazing angle corresponding to the probe source and $[\]^+$ is complex conjugation. Although $V(\theta_i)$ is normally a complex value, we assumed that the phase difference caused by the difference in grazing angles between θ_{0i} and θ_i is negligible and the phase changes caused by the bottom reflection are recovered by the two-way propagation of time-reversal processes.

Assume the array element spacing to be dense enough to be considered as a continuous array and the range from the array to the receiver to be much greater than the channel depth, $D \ll R$; then, the summation can be replaced by an integration²¹

$$p(l) \approx \frac{A}{2D} \int_{-\infty}^{\infty} \frac{|V(\theta)|^{|z|/D}}{ll_0} \exp jk(l - l_0) dz, \quad (10)$$

where z replaced the index i with $z = 2Di$, θ_i and l_{0i} are changed to θ and l_0 , respectively. The Fresnel approximation¹⁹ for the path length in Eq. (10) becomes

$$p(r, \varphi) = A \frac{\exp jk(r - r_0)}{2Drr_0} \int_{-\infty}^{\infty} |V(\theta)|^{|z|/D} \times \exp \left[jk \frac{z^2}{2} \left(\frac{\cos^2 \varphi}{r} - \frac{1}{r_0} \right) \right] \exp(jkz \sin \varphi) dz, \quad (11)$$

and the corresponding far-field beam-pattern expression is

$$D(\chi) = \int_{-\infty}^{\infty} |V(\theta)|^{|z|/D} \exp(j\chi z) dz, \quad (12)$$

where $\chi = k \sin \varphi$. Comparing Eq. (12) with the free-space beam pattern of Eq. (6), the factor from the bottom attenuation $|V(\theta)|^{|z|/D}$ serves as an aperture shading which eventually determines the effective aperture of the image array.

This image approach can be further extended to a range-dependent geometry, a wedge-shaped ocean. The slope of the bottom interface α is associated with the range to the apex R_a and the water depth D as $R_a \alpha \approx D$ (Fig. 9). A time-reversal mirror is located at the mouth of the wedge and a probe source at a range R . The probe signal propagates down slope to the array and the time-reversed signal is backpropagated up slope to the receiver. The main difference from the flat waveguide is that sound waves experience successive bottom reflections at incident angles 2α steeper (smaller) for up-slope (down-slope) propagation. Noting that the grazing angles for the first bounce and the last bounce are $\theta_i - \alpha$ and $\theta_i - (2i - 1)\alpha$, respectively, the mean bottom reflection coefficient for the i th image source is $V(\theta_i - \alpha i)$. The accumulated attenuation of the i th image source during the two-way

propagation is $V(\theta - \alpha i)^{2i}$. Using the relation of $2Di = z$, the corresponding far-field beam-pattern expression for a wedge ocean is

$$D(\chi) = \int_{-\infty}^{\infty} \left| V \left(\theta - \alpha \frac{|z|}{2D} \right) \right|^{|z|/D} \exp(j\chi z) dz, \quad (13)$$

where $\chi = k \sin \varphi$. Notice that the far-field beam pattern is modified by the waveguide geometry, which is realized through the change of the reflection coefficient.

IV. SPATIAL RESOLUTION OF AN ARRAY

A. Free space

In this section, we derive formulas describing the resolution of time-reversal arrays in free space. The transverse (Δ_z) resolution (breadth of focus) can be defined from the mainlobe width of the far-field beam pattern of Eq. (6). The solution of the beam-pattern function is

$$D(\varphi) = L \operatorname{sinc} \left(\frac{L \sin \varphi}{\lambda} \right), \quad (14)$$

where λ is the wavelength and L is the aperture. Following the conventional definition of the 3-dB beamwidth of the mainlobe ($\varphi_{3 \text{ dB}} \approx 0.886\lambda/L$), the transverse resolution is

$$\Delta_z = 0.886\lambda \frac{R}{L}, \quad (15)$$

where $\sin \varphi$ is approximated as φ and R is the range from the array.

Although the transverse focal structure is symmetric along the R axis, the longitudinal structure is not symmetric due to the r dependence in the near-field beam pattern. One method to define the longitudinal resolution is to examine the maximum range (r_{\max}) and the minimum range (r_{\min}) along the R axis within which there is a good focus with phase difference from the focal center ($R_0, 0$) less than $3\pi/4$. Since the maximum phase difference is caused by the end of the aperture ($\pm L/2$), the r_{\max} and r_{\min} can be defined from Eq. (5) as

$$r_{\max} \approx R_0 \left(1 + \frac{3\lambda}{L^2} R_0 \right), \quad (16)$$

$$r_{\min} \approx R_0 \left(1 - \frac{3\lambda}{L^2} R_0 \right). \quad (17)$$

Then, the longitudinal resolution ($\Delta_r = r_{\max} - r_{\min}$) expression becomes

$$\Delta_r = 6\lambda \left(\frac{R}{L} \right)^2. \quad (18)$$

The ranges of r_{\max} and r_{\min} roughly correspond to 3-dB down points in amplitude from the focal center. Although the proportionality constants needed in the above equations depend on the specific resolution criteria, for a given range (R) and wavelength (λ) the focal sizes in free space are directly proportional to the physical extent of the aperture (L) and the

square of the aperture (L^2) for the transverse and longitudinal directions, respectively.

B. Ocean waveguide

The resolution expression derived for free space can be used to define the resolution in an ocean waveguide. In the ocean, the effective aperture increases due to the multipath propagation caused by boundary reflections. Hence, the resolution increases over a free-space environment. The effective aperture is limited by the waveguide nature of acoustic propagation and attenuation in the bottom. For a lossless Pekeris waveguide of depth D , there exists a critical angle of reflection given by $\theta_c = \cos^{-1}(c_w/c_b)$ where c_w and c_b are the sound speeds in the water column and in the bottom, respectively. Sound propagating within the critical angle suffers no bottom loss and hence propagates to long distances. The length of the image array can be roughly written as

$$L_c \approx 2R \tan \theta_c, \quad (19)$$

and the corresponding resolution expressions are

$$\Delta_z \sim \frac{\lambda}{2 \tan \theta_c}, \quad (20)$$

$$\Delta_r \sim \frac{\lambda}{(2 \tan \theta_c)^2}. \quad (21)$$

For a lossy waveguide, we can use the far-field beam-pattern expression of Eq. (12) to derive resolution formulas. Although the integration in Eq. (12) can be evaluated numerically with any arbitrary reflection coefficient function $V(\theta)$, here we use a simple functional approximation of $V(\theta) \approx \exp(-\gamma\theta)$ to analytically solve the beam-pattern equation.²¹ Although a more complicated functional form would give a more accurate $V(\theta)$, $\exp(-\gamma\theta)$ is a good approximation for low grazing angle incidences and leads to closed-form expressions for resolution which are sufficient for the purpose of this paper for giving physical insight into how waveguide attenuation affects resolution or focal sizes associated with waveguide geometry. γ is an attenuation factor which can be determined by least-squares curve fitting for the known reflection coefficient curves with angles which would be obtained either from a geoacoustic model²⁰ or measured data.

With $V(\theta) \approx \exp(-\gamma\theta)$, the solution of the far-field beam pattern of Eq. (12) is (see the Appendix for details)

$$D(z) \sim \exp\left(-\frac{\gamma R}{4D} k^2 z^2\right). \quad (22)$$

The depth resolution for the 3-dB beamwidth can be defined as

$$\Delta_z = 0.374\lambda \sqrt{\frac{\gamma R}{D}}. \quad (23)$$

Using Eqs. (15) and (23), the corresponding linear, uniform array having the same 3-dB depth resolution would have an effective aperture

$$L_e = 2.368 \sqrt{\frac{DR}{\gamma}}. \quad (24)$$

From Eqs. (18) and (24), the range resolution in a lossy Pekeris waveguide would be

$$\Delta_r = 1.07\lambda \frac{\gamma R}{D}. \quad (25)$$

In a lossy waveguide, the resolution is a function of water depth D , medium attenuation γ , and range R . With the approximation of $V(\theta) \approx \exp(-\gamma\theta)$, the depth resolution (Δ_z) is found to be proportional to the square root of the attenuation factor γ and the range R , and the inverse square root of the waveguide depth D , while the range resolution (Δ_r) is proportional to the attenuation and the range and inversely proportional to the waveguide depth.

Using a similar approximation for the reflection coefficient in a wedge ocean, the far-field beam pattern of Eq. (13) becomes (see the Appendix for details)

$$D(z) \sim \exp\left[-\frac{\gamma R}{4D} \left(1 - \frac{R}{2R_a}\right) k^2 z^2\right]. \quad (26)$$

The corresponding depth and range resolution expressions are

$$\Delta_z = 0.374\lambda \sqrt{\frac{\gamma R}{D} \left(1 - \frac{R}{2R_a}\right)}, \quad (27)$$

$$\Delta_r = 1.07\lambda \frac{\gamma R}{D} \left(1 - \frac{R}{2R_a}\right). \quad (28)$$

A uniform array having the same 3-dB focal width would have an effective aperture

$$L_e = 2.368 \sqrt{\frac{DR}{\gamma(1 - R/2R_a)}}. \quad (29)$$

In a wedge ocean, an additional factor R_a is included for determining the image aperture which represents the geometry of the wedge ocean with depth D . This geometric factor results from the fact that each bounce of sound propagating from a probe source to a time-reversal array reduces the reflection angle by 2α . It is apparent from Fig. 9 that for an image interacting with the bottom in two-way transmission, the accumulated attenuation is smaller in a wedge ocean than in a flat ocean of constant depth D , which results in a larger image aperture in a wedge geometry. From the perspective of adiabatic modal propagation,²⁰ modes are compressed with up-slope propagation, which results in higher resolution for the time-reversal process in sloping environments.

C. Numerical example

Here, we present a numerical example of resolution calculation illustrating the depth and range resolution changes with range in a Pekeris waveguide and in a wedge ocean. In order to validate the accuracy of the results, we compare them with the focal sizes obtained with a parabolic equation full wave model.²² The model ocean consists of the pressure release surface, 100-m water column, and infinite bottom half space. The sound speeds are 1500 and 1600 m/s for the water and bottom, respectively, and the corresponding densities are 1.0 and 1.8 g/cm³. The bottom attenuation is 0.7

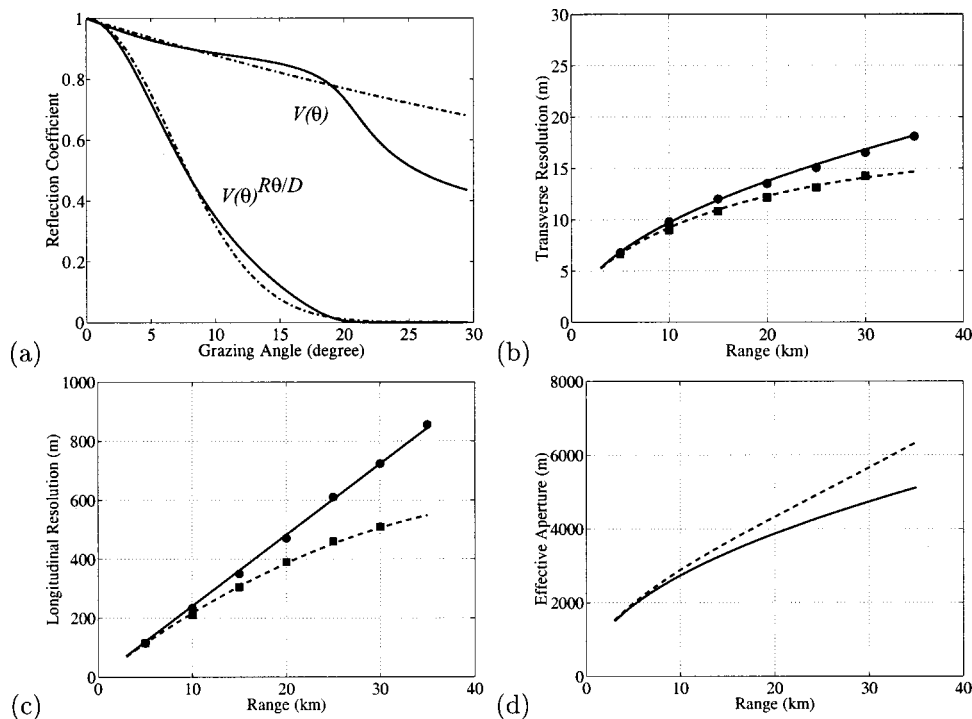


FIG. 10. An example of resolution calculation in a Pekeris waveguide and in a wedge ocean. The waveguide geometries are with $D=100$ m, $R_a=50$ km. The sound speeds are 1500 m/s and 1600 for water and bottom, respectively, and the corresponding densities are 1.0 and 1.8 g/cm³. The bottom attenuation is 0.7 dB/λ. (a) The calculated reflection coefficient $V(\theta)$ and the accumulated attenuation $V(\theta)^{R\theta/D}$ at 10-km range (solid line) and the approximation with $\exp(-\gamma\theta)$ (dot-dashed lines). (b) The depth resolution in a Pekeris waveguide (solid line) and in a wedge ocean (dashed line). The solid circles and squares are from simulation results with a parabolic equation model. (c) The range resolution. (d) The calculated effective apertures (L_e).

dB/λ. In a wedge ocean the water depth decreases from 100 to 0 m in a distance of 50 km having slope of 0.114°.

The resolution calculations are at 500-Hz and the corresponding wavelength is 3 m in the water column. Since the bottom is homogeneous, the reflection coefficient is independent of frequency. The solid line in Fig. 10(a) shows the reflection coefficient curve as a function of angle calculated with the geoacoustic properties. The dot-dashed line represents the approximation with $\exp(-\gamma\theta)$ where $\gamma=0.75$. Although there are some discrepancies between those two curves in $V(\theta)$ after the critical angle (20.4°), the difference turns out to be very small in the accumulated attenuation of $V(\theta)^{R\theta/D}$ due to the multiple interactions for the higher angle images. The overall effect on the pressure field from the difference would be negligible.

As shown in Figs. 10(b) and (c), the depth and range focal sizes increase with range due to the bottom attenuation. As expected, the focal sizes are smaller in the wedge ocean (dashed lines) than those in the flat ocean (solid lines) due to the geometric effect under the same geoacoustic conditions. The simulation results with a parabolic equation model²² (the solid circles and squares for the flat ocean and the wedge ocean, respectively) match well with the resolution curves obtained with the Eqs. (23), (25), (27), and (28), verifying the resolution equations derived in this paper for flat oceans as well as wedge oceans. The effective apertures (L_e) in Fig. 2(d) show that the aperture of the image array becomes much bigger than the physical extent of the array (100 m), resulting in finer resolution in a waveguide over the resolution in free space.

V. COMPARISON WITH MEASURED DATA

Here, we compare the resolution formulas with measured data. The main purpose is to describe the measured focal sizes along with their waveguide conditions: water

depth, range, and attenuation which are parametrized in the resolution formulation. The foci were realized with probe source depths at 60–80 m. For these depths, the focal structures of the high-frequency (3500-Hz) signals were stable for tens of minutes. The focal structures of the low-frequency (445-Hz) signals were stable for longer periods of time (several hours).^{3,4} Since the data collected for this comparison were from cases where the received probe-source pulse was retransmitted within a few minutes, we can assume that the foci were realized under relatively static ocean conditions. The resolution is defined as the focal size at the 3-dB down points from the peak signal level.

Figure 11(a) shows the comparison at 445-Hz in the Formiche area. The resolution curve is calculated with $\gamma=1.55$ and $D=110$ m. The attenuation factor γ is obtained by approximating the reflection coefficient as $V(\theta) \approx \exp(-\gamma\theta)$ which is calculated from the two-layer geoacoustic model for this area in Fig. 2(a). Since the effective modes contributing to the focal field are trapped below the thermocline, the effective waveguide depth²³ D is determined by removing the upper mixed layer (15 m) from the total water depth. The calculated resolution curve based on known geoacoustic parameters approximates closely the measured focal sizes. A numerical simulation⁴ using a normal-mode method also showed similar focal sizes for these 445-Hz data.

Figure 11(b) is at 3500-Hz in three different environments: the Formiche, flat Elba, and sloping Elba areas. The measured focal sizes are easily differentiated into three groups, with the largest focal size in the Formiche area and the smallest in the sloping Elba area for a given range. The calculated resolution curves match the measured data well with $\gamma=16$ and $D=115$ m for the Formiche area, with $\gamma=5$ and $D=90$ m for the flat Elba area, and with $\gamma=1.6$ and $D=90$ m for the sloping Elba area. The main difference in

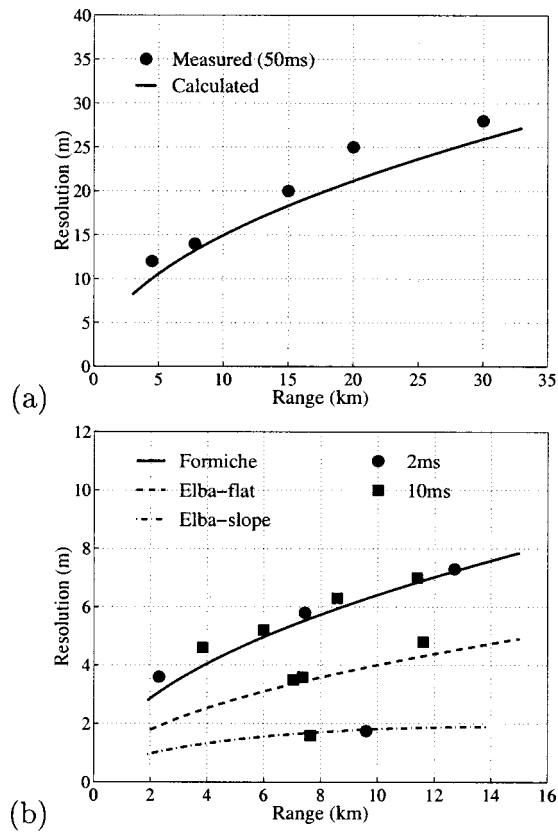


FIG. 11. Comparison between the measured vertical focal sizes and the calculated resolution based on the image aperture method with appropriate bottom attenuation: (a) for 445 Hz in the Formiche area with $\gamma=1.55$ and (b) for 3500 Hz in three different environments with $\gamma=16, 5, 1.6$ for the Formiche, flat Elba, and sloping Elba area, respectively.

effective depth between the Formiche area (115 m) and the Elba area (90 m) is due to the differences in the thermocline depth and the total water depth. The larger γ in the Formiche area indicates higher attenuation for waveguide propagation and larger focal sizes. The focal size is smaller in the sloping Elba area than that in the flat Elba area for the same γ due to the geometric effect in a sloping environment, but an additional adjustment of γ from 5 to 1.6 was needed to explain the measured data in the sloping area.

The attenuation factors ($\gamma=16$ for the Formiche area and $\gamma=5$ for the flat Elba area) used for the resolution calculation in Fig. 11(b) are larger than the values ($\gamma=7$ and $\gamma=1.5$, respectively) obtained from the geoacoustic models in Fig. 2. There can be several reasons for this mismatch. One of them is measurement error caused by range mismatch between the PS and the VRA. From the calculation with Eq. (25), the longitudinal focal sizes were about 300 and 100 m at 5-km range for the Formiche and Elba areas, respectively. During the experiment the PS was located within 50 m from the VRA in the Formiche area and 20 m in the Elba area. Although the focal size was affected by this range mismatch, the VRA was inside the focal zone. The other possible factor is the uncertainty in geoacoustic parameters. Since these geoacoustic models are based on low-frequency (<800 Hz) experiments,^{14,16} high-frequency sound propagation appears to experience different loss mechanisms. The frequency-dependent attenuation in layered sediment or additional loss

from rough boundary scattering²⁴ can be important in high-frequency propagation. Transmission loss measurements performed during the experiment also showed higher attenuation for 3500-Hz sound than attenuation values based on lower-frequency experiments in the area.

VI. SUMMARY

Acoustic foci realized with vertical time-reversal arrays in various shallow-water environments were presented and analyzed using an image aperture method. For a given frequency and range, the resolution is determined by waveguide attenuation and water depth in the ocean waveguide while the resolution is determined by the physical extent of the array in free space. With the approximation of $V(\theta) \approx \exp(-\gamma\theta)$ for the bottom reflection coefficient, the vertical focal size is found to be proportional to the square root of attenuation and inversely proportional to the square root of waveguide depth, while the horizontal focal size is found to be proportional to the attenuation and range and inversely proportional to the waveguide depth. In a sloping ocean, an additional geometric effect results in higher resolution for up-slope focusing.

ACKNOWLEDGMENTS

This research was supported by the Office of Naval Research, Contract No. N00014-94-1-0458.

APPENDIX: SOLUTIONS OF THE FAR-FIELD BEAM-PATTERN EQUATIONS

The accumulated attenuation for the two-way propagation between the probe source and i th image source are $V(\theta)^{2i}$ and $V(\theta - \alpha i)^{2i}$ for a flat ocean and a wedge ocean, respectively. Using the approximation $V(\theta) \approx \exp(-\gamma\theta)$ with relations of $2Di = z$, $R\theta \approx z$, and $R_a\alpha \approx D$, the attenuation expressions become $\exp(-\gamma z^2/RD)$ for a flat ocean and $\exp(-\gamma z^2(1 - R/2R_a)/RD)$ for a wedge ocean. Then, Eqs. (12) and (13) can be written as

$$D(\chi) = \int_{-\infty}^{\infty} \exp(-az^2) \exp(j\chi z) dz = \frac{1}{\sqrt{2a}} \exp\left(-\frac{\chi^2}{4a}\right), \quad (\text{A1})$$

where $a = \gamma/DR$ for a flat ocean and $a = \gamma(1 - R/2R_a)/DR$ for a wedge ocean, respectively, and $\chi = k \sin \varphi$. Noticing that $\varphi \approx Rz$, Eq. (A1) becomes

$$D(z) = \sqrt{\frac{DR}{2\gamma}} \exp\left(-\frac{\gamma R}{4D} k^2 z^2\right), \quad (\text{A2})$$

and

$$D(z) = \sqrt{\frac{DR}{2\gamma(1 - R/2R_a)}} \exp\left[-\frac{\gamma R}{4D} \left(1 - \frac{R}{2R_a}\right) k^2 z^2\right] \quad (\text{A3})$$

for a flat ocean and a wedge ocean, respectively.

- ¹M. Fink, "Time reversal mirrors," in *Acoustical Imaging*, edited by B. F. Jones (Plenum, New York, 1995), Vol. 25, pp. 1–15.
- ²M. Fink, "Time reversed acoustics," *Phys. Today* **50**, 34–40 (1997).
- ³W. A. Kuperman, W. S. Hodgkiss, H. C. Song, T. Akal, C. Ferla, and D. Jackson, "Phase conjugation in the ocean: Experimental demonstration of an acoustic time-reversal mirror," *J. Acoust. Soc. Am.* **102**, 25–40 (1998).
- ⁴W. S. Hodgkiss, H. C. Song, W. A. Kuperman, T. Akal, C. Ferla, and D. R. Jackson, "A long-range and variable focus phase conjugation experiment in shallow water," *J. Acoust. Soc. Am.* **105**, 1597–1604 (1999).
- ⁵T. Akal, G. Edelmann, S. Kim, W. S. Hodgkiss, W. A. Kuperman, and H. C. Song, "Low and high frequency ocean acoustic phase conjugation experiments," Proceedings of the Sixth European Conference of Underwater Acoustics, pp. 493–498 (2000).
- ⁶D. R. Jackson and D. R. Dowling, "Phase conjugation in underwater acoustics," *J. Acoust. Soc. Am.* **89**, 171–181 (1991).
- ⁷M. Born and E. Wolf, *Principles of Optics: Electromagnetic Theory of Propagation, Interference and Diffraction of Light* (Pergamon, New York, 1964), pp. 435–449.
- ⁸A. B. Baggeroer, W. A. Kuperman, and H. Schmidt, "Matched field processing: Source localization in correlated noise as an optimum parameter estimation problem," *J. Acoust. Soc. Am.* **83**, 571–587 (1988).
- ⁹P. Roux and M. Fink, "Time reversal in a waveguide: Study of the temporal and spatial focusing," *J. Acoust. Soc. Am.* **107**, 2418–2429 (2000).
- ¹⁰D. R. Dowling and D. R. Jackson, "Narrow-band performance of phase-conjugate arrays in dynamic random media," *J. Acoust. Soc. Am.* **91**, 3257–3277 (1992).
- ¹¹M. Dungan and D. R. Dowling, "Computed narrow-band time-reversing array retrofocusing in a dynamic shallow ocean," *J. Acoust. Soc. Am.* **107**, 3101–3112 (2000).
- ¹²T. Akal, "Bathymetry and bottom structure of zones near the island of Elba used for acoustical trials in shallow water," Technical Report, TM-162, SACLANT Undersea Research Centre, La Spezia, Italy, 1970.
- ¹³T. Akal, C. Gehin, B. Matteucci, and B. Tonarelli, "Measured and computed physical properties of sediment cores, island of Elba zone," Technical report, M-82, SACLANT Undersea Research Centre, La Spezia, Italy, 1972.
- ¹⁴J.-P. Hermand and P. Gerstoft, "Inversion of broad-band multitone acoustic data from the yellow shark summer experiments," *IEEE J. Ocean. Eng.* **21**, 324–346 (1996).
- ¹⁵D. F. Gingras and P. Gerstoft, "Inversion for geometric and geoacoustic parameters in shallow water: Experimental results," *J. Acoust. Soc. Am.* **97**, 3589–3598 (1995).
- ¹⁶F. B. Jensen, "Comparison of transmission loss data for different shallow water area with theoretical results provided by a three-fluid normal-mode propagation model," in *Sound Propagation in Shallow Water*, edited by O. F. Hastrup and O. V. Olesen (CP-14, SACLANT ASW Research Centre, La Spezia Italy, 1974), pp. 79–92.
- ¹⁷R. N. Bracewell, *The Fourier Transform and its Applications* (McGraw-Hill, New York, 1978), pp. 267–272.
- ¹⁸H. C. Song, P. R. Roux, and W. A. Kuperman, "Focal translation by frequency shift in free space," *IEEE Trans. Ultrason. Ferroelectr. Freq. Control* **47**, 687–695 (1999).
- ¹⁹L. J. Ziomek, "Three necessary conditions for the validity of the Fresnel phase approximation for the near-field beam pattern of an aperture," *IEEE J. Ocean Eng.* **18**, 73–75 (1993).
- ²⁰F. B. Jensen, W. A. Kuperman, M. B. Porter, and H. Schmidt, *Computational Ocean Acoustics* (American Institute of Physics, New York, 1994).
- ²¹L. E. Kinsler, A. R. Frey, A. B. Coppens, and J. V. Sanders, *Fundamentals of Acoustics* (Wiley, New York, 1982), pp. 427–430.
- ²²M. D. Collins, "Generalization of the split-step pade solution," *J. Acoust. Soc. Am.* **96**, 382–385 (1994).
- ²³F. B. Jensen and W. A. Kuperman, "Optimum frequency of propagation in shallow water environments," *J. Acoust. Soc. Am.* **73**, 1979–1984 (1983).
- ²⁴W. A. Kuperman and F. Ingenito, "Attenuation of the coherent component of sound propagating in shallow water with rough boundaries," *J. Acoust. Soc. Am.* **61**, 1178–1187 (1977).